



Ultra-low loss visible light waveguides for integrated atomic, molecular, and quantum photonics

NITESH CHAUHAN,¹ JIAWEI WANG,¹ DEBAPAM BOSE,¹ KAIKAI LIU,¹ R. L. COMPTON,² C. FERTIG,² C. W. HOYT,² AND DANIEL J. BLUMENTHAL^{1,*}

¹*Department of Electrical and Computer Engineering, University of California, Santa Barbara, Santa Barbara, CA 93106, USA*

²*Honeywell Aerospace, Plymouth, MN 55441, USA*

*danb@ucsb.edu

Abstract: Atomic, molecular and optical (AMO) visible light systems are the heart of precision applications including quantum, atomic clocks and precision metrology. As these systems scale in terms of number of lasers, wavelengths, and optical components, their reliability, space occupied, and power consumption will push the limits of using traditional laboratory-scale lasers and optics. Visible light photonic integration is critical to advancing AMO based sciences and applications, yet key performance aspects remain to be addressed, most notably waveguide losses and laser phase noise and stability. Additionally, a visible light integrated solution needs to be wafer-scale CMOS compatible and capable of supporting a wide array of photonic components. While the regime of ultra-low loss has been achieved at telecommunication wavelengths, progress at visible wavelengths has been limited. Here, we report the lowest waveguide losses and highest resonator Qs to date in the visible range, to the best of our knowledge. We report waveguide losses at wavelengths associated with strontium transitions in the 461 nm to 802 nm wavelength range, of 0.01 dB/cm to 0.09 dB/cm and associated intrinsic resonator Q of 60 Million to 9.5 Million, a decrease in loss by factors of 6x to 2x and increase in Q by factors of 10x to 1.5x over this visible wavelength range. Additionally, we measure an absorption limited loss and Q of 0.17 dB/m and 340 million at 674 nm. This level of performance is achieved in a wafer-scale foundry compatible Si₃N₄ platform with a 20 nm thick core and TEOS-PECVD deposited upper cladding oxide, and enables waveguides for different wavelengths to be fabricated on the same wafer with mask-only changes per wavelength. These results represent a significant step forward in waveguide platforms that operate in the visible, opening up a wide range of integrated applications that utilize atoms, ions and molecules including sensing, navigation, metrology and clocks.

© 2022 Optica Publishing Group under the terms of the [Optica Open Access Publishing Agreement](#)

1. Introduction

Photonic integration can improve the reliability, reduce the cost and size, and enable scalability, of traditionally table-top sized precision lasers and optics for visible light applications such as optical atomic clocks [1–3], precision spectroscopy [4,5] and metrology [6,7], atomic sensors [8–10], and quantum information sciences and applications [11–14]. For example, atomic, molecular and optic (AMO) applications [15] rely on racks of lasers and table-sized optics to perform spectroscopy, trap and cool, manipulate, and probe just a single atom, ion, molecule or quantum gate. Today's optics infrastructure presents challenges to scaling the number of atoms, ions or qubits, in order to improve the sensitivity of a quantum sensor or computational complexity of a quantum computer. For AMO systems, waveguide loss is paramount to the preservation of photons and resonator Q plays a critical role in laser linewidth narrowing, phase noise reduction and filtering. Photonic integration can address these requirements [5,16] and key

functions including photon routing, optical filtering [17], free-space beam formation [12,18–20], and hybrid tunable [21,22] and ultra-low linewidth lasers [23,24]. Realizing a wafer-scale, CMOS compatible, photonic integration platform that delivers ultra-low waveguide losses (< 0.1 dB/cm) and ultra-high Q resonators (> 10 Million) across the 400 - 900 nm range is critical to realize these advances.

The choice of waveguide core material, in part, will determine the loss and Q in the 400 - 900 nm wavelength range [25] as well as waveguide design and processing considerations [26]. Wide bandgap waveguide core material choices suited to the visible include silicon nitride (Si_3N_4), aluminum nitride (AlN), alumina (Al_2O_3), tantalum (Ta_2O_5), lithium niobate (LiNbO_3), titanium dioxide (TiO_2), silicon dioxide (SiO_2) and diamond [23,26–43]. In addition to the waveguide core bandgap, nonlinear absorption, intrinsic material absorption in the cladding and substrate, and waveguide side- and top-wall scattering must be addressed when designing for this wavelength regime. Since scattering loss scales as $1/\lambda^4$ it contributes significantly at the lower end of the visible spectrum. To date, the lowest losses reported are 0.06 dB/cm in Si_3N_4 and LiNbO_3 at $\lambda = 634$ nm and 637 nm respectively [34,41], 0.22 dB/cm at 453 nm and 0.93 dB/cm at 405 nm in Si_3N_4 [27], and 0.6 dB/cm at $\lambda = 458$ nm in Al_2O_3 [33,35]. Resonator Qs in the visible have been mostly been relegated to sub-Million [34] with a record-high 11 million reported at $\lambda = 637$ nm in LiNbO_3 and recently 6 million at 453 nm in Si_3N_4 [27]. Improving visible light waveguide losses and resonator Qs will enable integration of key functions for atom, ion and molecule science, new physics and their applications.

Here, we report the lowest waveguide losses and highest Qs demonstrated in any wafer-scale integrated waveguide platform to date in the wavelength range 461 nm - 802 nm, specifically for strontium atomic transitions, to the best of our knowledge. The waveguides and devices are fabricated using a wide bandgap (> 405 nm) [25], CMOS compatible waveguide design, based on a 20 nm thick LPCVD Si_3N_4 core, a thermal SiO_2 lower cladding, and a TEOS-PECVD deposited upper cladding. We report losses of 0.01 dB/cm (1 dB/m) at 674 nm and 698 nm, 0.02 dB/cm (2 dB/m) at 802 nm, and 0.09 dB/cm (9 dB/m) at 461 nm. These results represent a 6x decrease in loss over the prior lowest reported red/NIR waveguide losses [33,35,41] and a 2x loss decrease in the blue [27]. We also report the highest resonator Qs in the 461 nm – 802 nm wavelength range to date, 60 million at $\lambda = 698$ nm, 54.4 Million at $\lambda = 674$ nm, 28 Million at $\lambda = 802$ nm and 9.5 Million at $\lambda = 461$ nm, representing a 10x increase at 802 nm, a 5x increase at 674 nm/698 nm [32,35,41] and a 1.5x increase over the prior state of the art in blue [27]. We compare the losses from resonators at 461 nm and 698 nm with losses from 2 m coils [28].

An illustrative example of how ultra-low loss waveguides and ultra-high Q resonators, as well as other photonic structures, can be applied to an atomic or ion application (e.g. quantum, spectroscopy, clocks, computation) such as an integrated strontium atom cooling and clock application (Fig. 1). This example can leverage ultra-low loss waveguide technology to realize extended cavity tunable lasers [21], visible light emission ultra-narrow linewidth stimulated Brillouin scattering (SBS) lasers [23,24] and integrated reference cavities [44]. For example, beams can be converted from ultra-low loss waveguides to magneto optical trap (MOT) cooling beams using large area surface gratings [18]. Other potential applications include an ion trap [45,46], quantum computation [45], Rydberg blockade gates [46] and Rydberg sensors [11].

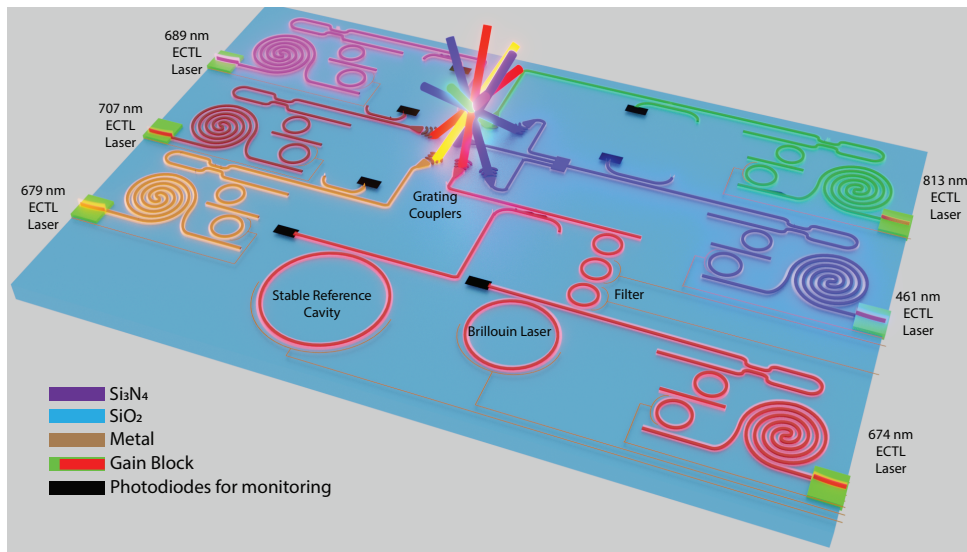


Fig. 1. Illustrative example application of visible light ultra-low loss photonic integrated waveguides and ultra-high Q resonators to generate and deliver neutral Sr atom cooling and clock transition beams.

2. Waveguides and resonators

The waveguides are fabricated using a wafer-scale CMOS compatible LPCVD deposited Si_3N_4 core fabrication process whose bandgap is optically transparent at wavelengths above 405 nm [26]. Our design employs an optimized waveguide geometry to minimize the losses in the 461 nm to 802 nm wavelength range while providing reasonably tight bend radii for all the wavelengths ($<10^{-4}$ dB/cm contribution from bend for radius > 0.33 mm for blue, > 2.3 mm for red and > 5.5 mm for 802 nm). A 20 nm Si_3N_4 thick core is selected to support a large mode volume and low mode overlap (< 0.1) to minimize side- and top-wall scattering losses as well as waveguide core absorption loss. To optimize loss and footprint at each wavelength, the waveguide width is adjusted using mask-only design changes. This approach enables multiple visible wavelengths with a common nitride core thickness to be integrated. The waveguide width of 1.3 μm at $\lambda = 461$ nm minimizes loss and supports a single TE mode. At $\lambda = 674$ nm and $\lambda = 698$ nm a 2.3 μm width minimizes loss and supports a quasi-single TE mode with a weakly guided TM mode that is filtered out using appropriate filter bend radii < 10 mm [47]. The 2.3 μm width supports single mode at 802 nm. The upper and lower cladding thicknesses are 6 μm and 15 μm respectively. Figure 2 shows the waveguide cross section and mode profiles at the 4 wavelengths. Further details of the waveguide design are given in the supplementary materials.

We measure the intrinsic and loaded Qs of all-pass ring resonators and derive the waveguide losses and absorption limited loss from these measurements (described later in this paper). Spiral coils are used to measure propagation losses directly, and we compare the losses obtained using these two approaches. A 3 mm radius resonator is used for Q measurement at 461 nm (Fig. 3(a)) and 2 meter coil is used for propagation loss measurements at 450 nm (Fig. 3(d)). A 9.4 mm radius resonator is used for Q measurement at 698 nm (Fig. 3(b)) and 2 meter coil is used for propagation loss measurements at 698 nm (Fig. 3(c)). At the other wavelengths, we designed and fabricated resonators with 8.9 mm radius for $\lambda = 674$ nm, and 10 mm radius for $\lambda = 802$ nm. The resonator power coupling factor (κ^2) is $\sim 16\%$ at $\lambda = 461$ nm, 1.5% at $\lambda = 674$ nm, 1% at $\lambda = 698$ nm and 57%, at $\lambda = 802$ nm. The resonators are designed to be over-coupled for 461 nm and 802 nm,

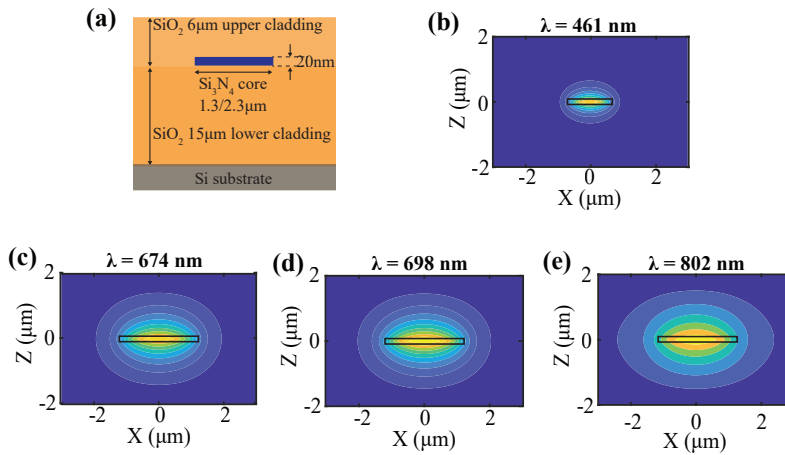


Fig. 2. Waveguide cross section and mode profiles: (a) Cross section of waveguide with core and cladding dimensions. (b) Mode profile at $\lambda = 461 \text{ nm}$ in a 1.3 μm wide waveguide with mode area = $0.7 \mu\text{m}^2$ and confinement factor = 0.065. (c) Mode profile at $\lambda = 674 \text{ nm}$ in a 2.3 μm wide waveguide with mode area = $3 \mu\text{m}^2$ and confinement factor = 0.031. (d) Mode profile for $\lambda = 698 \text{ nm}$ with mode area = $3.3 \mu\text{m}^2$ and confinement factor = 0.028. (e) Mode profile at $\lambda = 802 \text{ nm}$ in a 2.3 μm wide waveguide with mode area = $5.1 \mu\text{m}^2$ and confinement factor = 0.020.

critically coupled for 674 nm, and under-coupled for 698 nm. Test structures are employed to independently measure κ^2 , and are used with the Q measurements to extract loss from resonators.

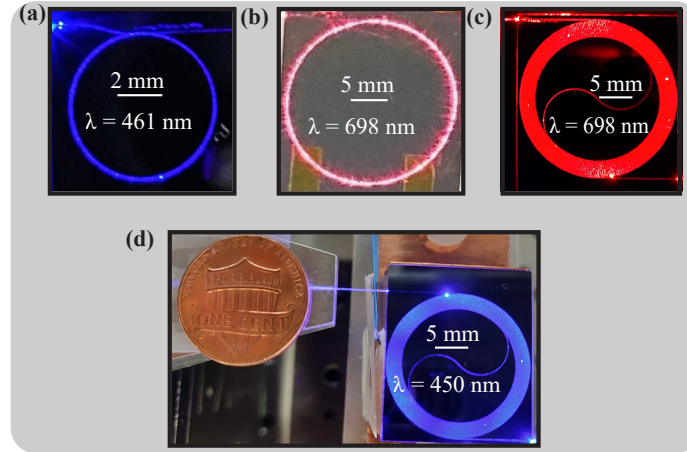


Fig. 3. Structures for waveguide loss measurements: (a) $R = 3 \text{ mm}$ resonator for 461 nm Q measurement (b) $R = 9.4 \text{ mm}$ resonator for 698 nm Q measurement (c) 2 m coil for measuring propagation loss at 698 nm (d) 2 m coil for measuring propagation loss at 450 nm with a penny for size comparison.

3. Results

We measured the Q at $\lambda = 674 \text{ nm}$ and $\lambda = 802 \text{ nm}$ using a frequency-swept source that was calibrated by an unbalanced Mach Zehnder interferometer (MZI) method [23,26]. The Q at $\lambda = 461 \text{ nm}$ and $\lambda = 698 \text{ nm}$ was measured by using a swept source that was calibrated by adding

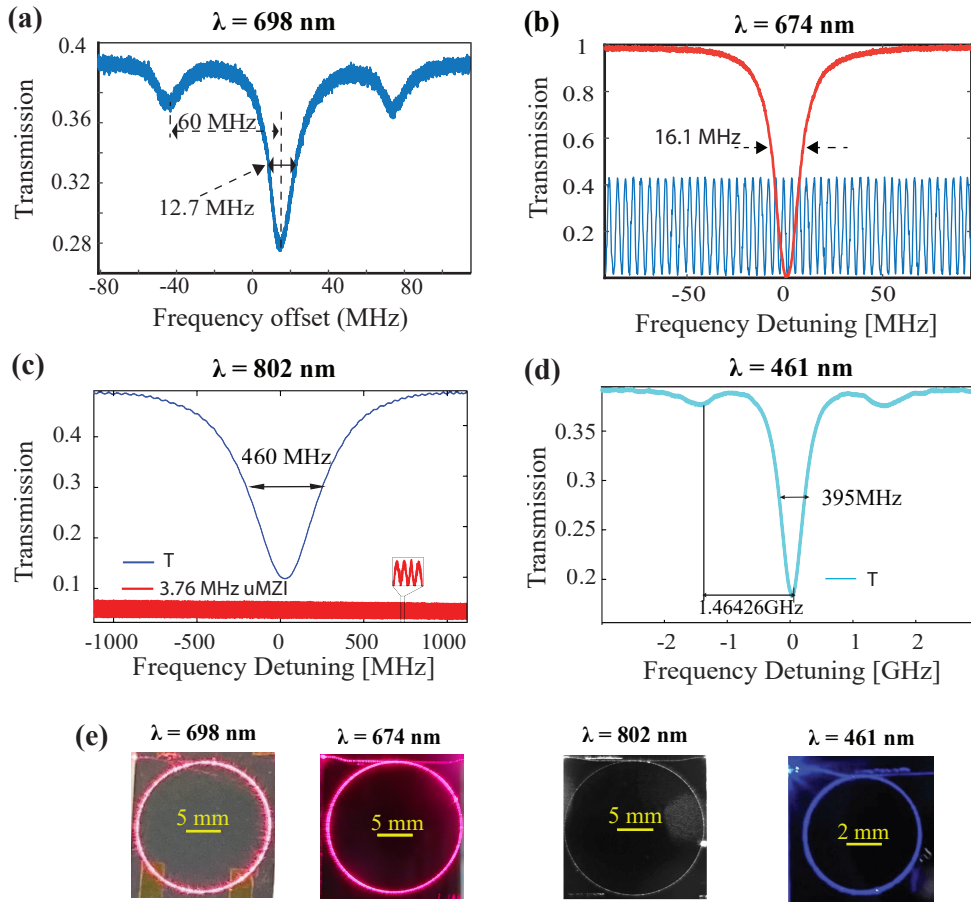


Fig. 4. Q Measurements: (a) T is resonator transmission spectrum, Q measurement for ring of $R = 9.4 \text{ mm}$, loaded $Q = 34.4$ million and intrinsic $Q = 60$ million at $\lambda = 698 \text{ nm}$. (b) Q measurement for ring of $R = 8.9 \text{ mm}$, loaded $Q = 27.7$ million and intrinsic $Q = 54.4$ million at $\lambda = 674 \text{ nm}$. (c) Q measurement for ring of $R = 10 \text{ mm}$, loaded $Q = 0.81$ million and intrinsic $Q = 28$ million at $\lambda = 802 \text{ nm}$. (d) Q measurement for ring of $R = 3 \text{ mm}$, loaded $Q = 1.65$ million and intrinsic $Q = 9.5$ million at $\lambda = 461 \text{ nm}$ (e) Images of resonators during Q measurements, the bright spot in 802 nm resonator is a particle in vicinity of waveguide.

sidebands at a known frequency offset from the carrier and then sweeping the carrier as well as the sidebands across the resonance [26]. We calibrate the MZI and have found in our previous works that Q values obtained using MZI and sideband methods match well with values obtained from cavity ring-down measurements [25,49]. Loss is extracted from resonators Qs and coupling coefficients from test structures. Figure 4 shows the frequency sweeps of the resonators for extracting Q. Intrinsic Q is dependent on the resonator loss only as intrinsic gives a limit to Q. Loaded Q is when the resonator is coupled to a bus and includes coupling losses and is the Q used in applications.

At $\lambda = 698 \text{ nm}$, the intrinsic $Q = 60$ million and loaded $Q = 34.4$ million (Fig. 4(a)) are measured with a corresponding calculated 0.01 dB/cm (1 dB/m) loss. At $\lambda = 674 \text{ nm}$, the intrinsic $Q = 54.4$ million and loaded $Q = 27.7$ million (Fig. 4(b)) with a corresponding 0.01 dB/cm (1 dB/m) loss. At $\lambda = 802 \text{ nm}$ the intrinsic $Q = 28.3$ million and loaded $Q = 0.81$ million (Fig. 4(c)), corresponding to a 0.02 dB/cm (2 dB/m) propagation loss. At $\lambda = 461 \text{ nm}$, the loaded $Q = 1.65$

million and intrinsic $Q = 9.5$ million (Fig. 4(d)) with a corresponding 0.09 dB/cm (9 dB/m) loss. At $\lambda = 698$ nm, the propagation loss measured using the spiral (Fig. 3(c)) is 0.03 dB/cm (3 dB/m). We believe the mismatch at $\lambda = 698$ nm between the resonator and spiral loss is due to the increased number of particles on the spiral waveguides as compared to the resonators. At 802 nm, we believe the loss is also increased due to particles as seen in the right portion of the 802 nm resonator in Fig. 4(e). The propagation loss at $\lambda = 450$ nm is 0.08 dB/cm (8 dB/m), obtained from the spiral in Fig. 3(d), [28] which matches well with calculated 0.09 dB/cm (9 dB/m) loss from resonator at $\lambda = 461$ nm. The fiber to chip coupling losses are 3 dB/facet at $\lambda = 461$ nm, 4.5 dB/facet at $\lambda = 674$ nm, and 3.5 dB/facet at $\lambda = 802$ nm. These coupling losses can be improved by utilizing mode size converters at the facets and polishing of facets [48].

We measure the absorption loss at 674 nm to separate the contributions of absorption and scattering losses and determine the potential loss and Q given the scattering loss is reduced to below absorption. This measurement follows a technique to quantify the resonance photothermal induced bistable linewidth shift [26] using a spectral scan across resonance with a high on-chip power induces a photothermal resonance redshift that is comparable to the resonance linewidth. This photothermal effect is a direct result of absorption heating in the resonator. As shown in Fig. 5(a), the red detuning (from shorter wavelength to longer wavelength) across resonance heats up the resonator and induces a resonance redshift, resulting in a skewed lineshape. To extract the absorption loss relative to the total loss, we simulate the thermal impedance of the ring resonator in Comsol. Assuming $R_{th} = 9.72$ K/W, we measure the thermal-optic redshift with a global heating of the chip, $\Delta f_{res}/\Delta T = 9.31$ GHz/K, which yields the resonance redshift per milliwatt of optical power absorbed by the resonator, $\Delta f_{res}/P_{abs} = 38.0$ MHz/mW. As shown in Fig. 5(b), the resonance redshift has a linear relationship with on-chip power, confirming the photothermal heating effect, from which we extract the absorption loss to be 0.17 dB/m which is $< 15\%$ of total loss. The intrinsic Q corresponding to this absorption loss is ~ 340 million at $\lambda = 674$ nm. This shows our losses are scattering limited in red with $> 85\%$ contribution from scattering and further improvements in losses to below < 1 dB/m and Q 's in excess of 100 million at red are possible by reducing the sidewall scattering.

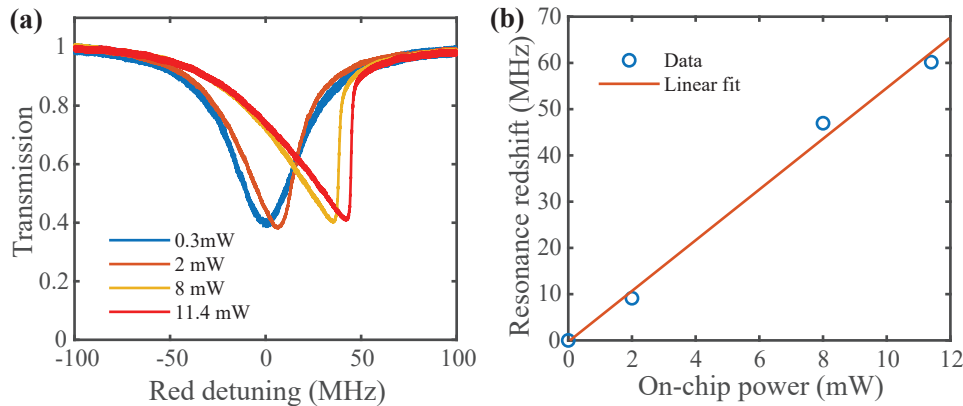


Fig. 5. Thermal bistability measurement (a) Resonance transmission at different on-chip powers (power in the bus waveguide) showing thermal redshift (b) Rate of resonance redshift from fit = 5.4 MHz/mW.

A summary of published losses and Q values across this wavelength range for different waveguide material systems are shown in Fig. 6(a) and (b), respectively for wavelength range 450 nm – 802 nm. Our measured losses are ~ 2 - 6 times lower than the best previously reported in

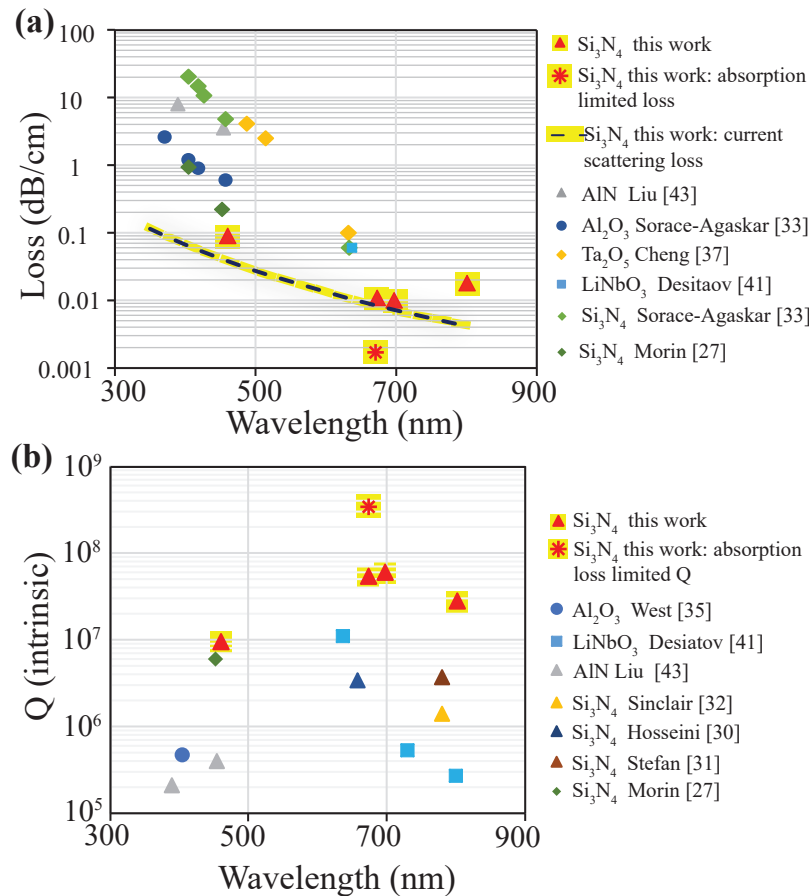


Fig. 6. (a) Waveguide loss summary for different published waveguide materials compared to our results (\blacktriangle) including the absorption limited loss (*). The dotted line shows the Rayleigh scattering loss scaling which indicates the limit of scattering loss achievable for our current fabrication process and design. The higher loss at $\lambda = 802$ nm is due to the particle as discussed earlier while higher loss at $\lambda = 461$ nm might either be due to higher absorption loss or particles. The dotted line gives a rough estimate of losses expected at wavelengths other than the ones reported in this paper for our waveguide platform. (b) Summary of intrinsic Q values in different waveguide materials compared to our results (\blacktriangle) and absorption loss limited Q (*). The absorption limited loss is less than the current waveguide scattering loss due to sidewall scattering. Improvement towards the absorption limited loss and Q is possible by reducing the scattering losses to below these values.

any material platform and our reported Qs are 10x higher at NIR, 5x higher at red wavelengths and 1.5x higher in the blue than previously reported best values.

4. Conclusions and discussion

We report the lowest demonstrated waveguide losses in the visible and near IR region between 0.01 dB/cm and 0.09 dB/cm, for any waveguide platform to the best of our knowledge. We also report the highest Qs for a bus-coupled ring resonator, between ~ 10 million and 60 million, in this same wavelength range. This CMOS compatible, wafer-scale integration platform opens the

possibility for on-chip components like delay lines, switches, Brillouin lasers, reference cavities, tunable lasers and more, to support visible light AMO applications including quantum, atom, ion and molecule transitions. The low absorption limited loss at 674 nm (0.17 dB/m, <15% of total loss) shows the potential to further improve these results by advanced fabrication processes that reduce the roughness of sidewalls [26]. There are opportunities to further reduce the loss to below 1 dB/meter and the Q to greater than 300 million by employing nitride surface passivation and blanket nitride deposition techniques [26]. These results represent a significant step forward in visible light wafer-scale photonic integration platforms, opening a wide range of potential applications that utilize atoms, ions and molecules including sensing, navigation, metrology and clocks.

Funding. Defense Advanced Research Projects Agency (FA9453-19-C-0030); Advanced Research Projects Agency - Energy (DE-AR0001042).

Acknowledgments. The authors would like to thank Nick Hutzler, Department of Physics, Caltech and David Weld, Department of Physics, UCSB for useful discussions. The authors would also like to thank Jim Nohava and Karl Nelsen at Honeywell for help with upper cladding deposition and annealing of devices.

Disclosures. The authors declare no conflicts of interest.

Data availability. The data that support the findings of this study are available from the corresponding author upon reasonable request.

Supplemental document. See [Supplement 1](#) for supporting content.

References

1. A. Ludlow, "The Strontium Optical Lattice Clock: Optical Spectroscopy with Sub-Hertz Accuracy," *40*, OPC.10 (2009).
2. B. J. Bloom, T. L. Nicholson, J. R. Williams, S. L. Campbell, M. Bishof, X. Zhang, W. Zhang, S. L. Bromley, and J. Ye, "An optical lattice clock with accuracy and stability at the 10–18 level," *Nature* **506**(7486), 71–75 (2014).
3. A. D. Ludlow, T. Zelevinsky, G. K. Campbell, S. Blatt, M. M. Boyd, M. H. G. de Miranda, M. J. Martin, J. W. Thomsen, S. M. Foreman, J. Ye, T. M. Fortier, J. E. Stalmaker, S. A. Diddams, Y. L. Coq, Z. W. Barber, N. Poli, N. D. Lemke, K. M. Beck, and C. W. Oates, "Sr Lattice Clock at 1 × 1805–1808 Fractional Uncertainty by Remote Optical Evaluation with a Ca Clock," *Science* **319**(5871), 1805–1808 (2008).
4. S. Borri and G. Santambrogio, "Laser spectroscopy of cold molecules," *Adv. Phys.: X* **1**, 368–386 (2016).
5. C. W. Chou, A. L. Collopy, C. Kurz, Y. Lin, M. E. Harding, P. N. Plessow, T. Fortier, S. Diddams, D. Leibfried, and D. R. Leibrandt, "Frequency-comb spectroscopy on pure quantum states of a single molecular ion," *Science* **367**(6485), 1458–1461 (2020).
6. J. Ye, H. J. Kimble, and H. Katori, "Quantum State Engineering and Precision Metrology Using State-Insensitive Light Traps," *Science* **320**(5884), 1734–1738 (2008).
7. J. Levine, "Introduction to time and frequency metrology," *Rev. Sci. Instrum.* **70**(6), 2567–2596 (1999).
8. J. Kitching, S. Knappe, and E. A. Donley, "Atomic Sensors – A Review," *IEEE Sensors J.* **11**(9), 1749–1758 (2011).
9. M. de Angelis, A. Bertoldi, L. Cacciapuoti, A. Giorgini, G. Lamporesi, M. Prevedelli, G. Saccorotti, F. Sorrentino, and G. M. Tino, "Precision gravimetry with atomic sensors," *Meas. Sci. Technol.* **20**(2), 022001 (2009).
10. D. H. Meyer, Z. A. Castillo, K. C. Cox, and P. D. Kunz, "Assessment of Rydberg Atoms for Wideband Electric Field Sensing," *J. Phys. B: At., Mol. Opt. Phys.* **53**(3), 034001 (2020).
11. H. Levine, A. Keesling, A. Omran, H. Bernien, S. Schwartz, A. S. Zibrov, M. Endres, M. Greiner, V. Vuletić, and M. D. Lukin, "High-Fidelity Control and Entanglement of Rydberg-Atom Qubits," *Phys. Rev. Lett.* **121**(12), 123603 (2018).
12. R. J. Niffenegger, J. Stuart, C. Sorace-Agaskar, D. Kharas, S. Bramhavar, C. D. Bruzewicz, W. Loh, R. T. Maxson, R. McConnell, D. Reens, G. N. West, J. M. Sage, and J. Chiaverini, "Integrated multi-wavelength control of an ion qubit," *Nature* **586**(7830), 538–542 (2020).
13. A. W. Elshaari, W. Pernice, K. Srinivasan, O. Benson, and V. Zwiller, "Hybrid integrated quantum photonic circuits," *Nat. Photonics* **14**(5), 285–298 (2020).
14. J. Wang, F. Sciarrino, A. Laing, and M. G. Thompson, "Integrated photonic quantum technologies," *Nat. Photonics* **14**(5), 273–284 (2020).
15. J. M. Pino, J. M. Dreiling, C. Figgatt, J. P. Gaebler, S. A. Moses, M. S. Allman, C. H. Baldwin, M. Foss-Feig, D. Hayes, K. Mayer, C. Ryan-Anderson, and B. Neyenhuis, "Demonstration of the trapped-ion quantum CCD computer architecture," *Nature* **592**(7853), 209–213 (2021).
16. Y. Lin, D. R. Leibrandt, D. Leibfried, and C. Chou, "Quantum entanglement between an atom and a molecule," *Nature* **581**(7808), 273–277 (2020).

17. T. A. Huffman, G. M. Brodnik, C. Pinho, S. Gundavarapu, D. Baney, and D. J. Blumenthal, "Integrated Resonators in an Ultralow Loss Si3N4/SiO₂Platform for Multifunction Applications," *IEEE J. Sel. Top. Quantum Electron.* **24**(4), 1–9 (2018).
18. N. Chauhan, D. Bose, M. Puckett, R. Moreira, K. Nelson, and D. J. Blumenthal, "Photonic Integrated Si3N4 Ultra-Large-Area Grating Waveguide MOT Interface for 3D Atomic Clock Laser Cooling," in *Conference on Lasers and Electro-Optics* (OSA, 2019), p. STu4O.3.
19. M. T. Hummon, S. Kang, D. G. Bopp, Q. Li, D. A. Westly, S. Kim, C. Fredrick, S. A. Diddams, K. Srinivasan, V. Aksyuk, and J. E. Kitching, "Photonic chip for laser stabilization to an atomic vapor with 10⁻¹¹ instability," *Optica* **5**(4), 443–449 (2018).
20. C. Ropp, C. Ropp, A. Yulaev, A. Yulaev, D. Westly, G. Simelgor, and V. Aksyuk, "Meta-grating outcoupplers for optimized beam shaping in the visible," *Opt. Express* **29**(10), 14789–14798 (2021).
21. Y. Lin, C. Browning, R. B. Timens, D. H. Geuzebroek, C. G. H. Roeloffzen, D. Geskus, R. M. Oldenbeuving, R. G. Heideman, Y. Fan, K. J. Boller, J. Zhao, and L. P. Barry, "Narrow linewidth hybrid InP-TriPleX photonic integrated tunable laser based on silicon nitride micro-ring resonators," in *Optical Fiber Communication Conference* (OSA, 2018), p. Th2A.14.
22. M. A. Tran, D. Huang, J. Guo, T. Komljenovic, P. A. Morton, and J. E. Bowers, "Ring-Resonator Based Widely-Tunable Narrow-Linewidth Si/InP Integrated Lasers," *IEEE J. Sel. Top. Quantum Electron.* **26**(2), 1–14 (2020).
23. S. Gundavarapu, G. M. Brodnik, M. Puckett, T. Huffman, D. Bose, R. Behunin, J. Wu, T. Qiu, C. Pinho, N. Chauhan, J. Nohava, P. T. Rakich, K. D. Nelson, M. Salit, and D. J. Blumenthal, "Sub-hertz fundamental linewidth photonic integrated Brillouin laser," *Nat. Photonics* **13**(1), 60–67 (2019).
24. N. Chauhan, A. Isichenko, K. Liu, J. Wang, Q. Zhao, R. O. Behunin, P. T. Rakich, A. M. Jayich, C. Fertig, C. W. Hoyt, and D. J. Blumenthal, "Visible light photonic integrated Brillouin laser," *Nat. Commun.* **12**(1), 4685 (2021).
25. D. J. Blumenthal, "Photonic integration for UV to IR applications," *APL Photonics* **5**(2), 020903 (2020).
26. M. W. Puckett, K. Liu, N. Chauhan, Q. Zhao, N. Jin, H. Cheng, J. Wu, R. O. Behunin, P. T. Rakich, K. D. Nelson, and D. J. Blumenthal, "422 Million intrinsic quality factor planar integrated all-waveguide resonator with sub-MHz linewidth," *Nat. Commun.* **12**(1), 934 (2021).
27. T. J. Morin, L. Chang, W. Jin, C. Li, J. Guo, H. Park, M. A. Tran, T. Komljenovic, and J. E. Bowers, "CMOS-foundry-based blue and violet photonics," *Optica* **8**(5), 755–756 (2021).
28. N. Chauhan, J. Wang, D. Bose, R. Moreira, and D. J. Blumenthal, "Ultra-Low Loss 698 nm and 450 nm Silicon Nitride Visible Wavelength Waveguides for Strontium Atomic Clock Applications," in *Conference on Lasers and Electro-Optics* (2020), Paper STh1J.2 (Optical Society of America, 2020), p. STh1J.2.
29. A. Raza, S. Clemmen, P. Wuytens, M. de Goede, A. S. K. Tong, N. Le Thomas, C. Liu, J. Suntivich, A. G. Skirtach, S. M. Garcia-Blanco, D. J. Blumenthal, J. S. Wilkinson, and R. Baets, "High index contrast photonic platforms for on-chip Raman spectroscopy," *Opt. Express* **27**(16), 23067 (2019).
30. E. S. Hosseini, S. Yegnanarayanan, A. H. Atabaki, M. Soltani, and A. Adibi, "High Quality Planar Silicon Nitride Microdisk Resonators for Integrated Photonics in the VisibleWavelength Range," *Opt. Express* **17**(17), 14543–14551 (2009).
31. L. Stefan, M. Bernard, R. Guider, G. Pucker, L. Pavese, and M. Ghulinyan, "Ultra-high-Q thin-silicon nitride strip-loaded ring resonators," *Opt. Lett.* **40**(14), 3316 (2015).
32. M. Sinclair, M. Sinclair, K. Gallacher, M. Sorel, J. C. Bayley, E. McBrearty, R. W. Millar, S. Hild, and D. J. Paul, "1.4 million Q factor Si₃N₄ micro-ring resonator at 780 nm wavelength for chip-scale atomic systems," *Opt. Express* **28**(3), 4010–4020 (2020).
33. C. Sorace-Agaskar, S. Bramhavar, D. Kharas, W. Loh, P. W. Juodawlkis, J. Chiaverini, and J. M. Sage, "Multi-layer integrated photonics from the ultraviolet to the infrared," *Proc. SPIE* **10510**, 105100D (2018).
34. S. Bramhavar, C. Sorace-Agaskar, D. Kharas, W. Loh, R. Maxson, G. N. West, R. Niffenegger, P. W. Juodawlkis, J. Chiaverini, and J. M. Sage, "A visible-light integrated photonic platform for atomic systems," *Proc. SPIE* **10921**, 109211D (2019).
35. G. N. West, W. Loh, D. Kharas, C. Sorace-Agaskar, K. K. Mehta, J. Sage, J. Chiaverini, and R. J. Ram, "Low-loss integrated photonics for the blue and ultraviolet regime," *APL Photonics* **4**(2), 026101 (2019).
36. M. Soltani, R. Soref, T. Palacios, and D. Englund, "AlGaN/AlN integrated photonics platform for the ultraviolet and visible spectral range," *Opt. Express* **24**(22), 25415–25423 (2016).
37. Y. C. Cheng and W. D. Festwood, "Losses in tantalum pentoxide waveguides," *J. Electron. Mater.* **3**(1), 37–50 (1974).
38. R. Fan, C.-L. Wu, Y.-Y. Lin, C.-Y. Liu, P.-S. Hwang, C.-W. Liu, J. Qiao, M.-H. Shih, Y.-J. Hung, Y.-J. Chiu, A.-K. Chu, and C.-K. Lee, "Visible to near-infrared octave spanning supercontinuum generation in tantalum pentoxide (Ta₂O₅) air-cladding waveguide," *Opt. Lett.* **44**, 1512–1515 (2019).
39. M. Belt, M. L. Davenport, J. E. Bowers, and D. J. Blumenthal, "Ultra-low-loss Ta₂O₅-core/SiO₂-clad planar waveguides on Si substrates," *Optica* **4**(5), 532–536 (2017).
40. A. Boes, B. Corcoran, L. Chang, J. Bowers, and A. Mitchell, "Status and Potential of Lithium Niobate on Insulator (LNOI) for Photonic Integrated Circuits," *Laser Photonics Rev.* **12**(4), 1700256 (2018).
41. B. Desiatov, A. Shams-Ansari, M. Zhang, C. Wang, and M. Lončar, "Ultra-low-loss integrated visible photonics using thin-film lithium niobate," *Optica* **6**(3), 380–384 (2019).
42. C. C. Evans, C. Liu, and J. Suntivich, "Low-loss titanium dioxide waveguides and resonators using a dielectric lift-off fabrication process," *Opt. Express* **23**(9), 11160–11169 (2015).

43. X. Liu, A. W. Bruch, Z. Gong, J. Lu, J. B. Surya, L. Zhang, J. Wang, J. Yan, and H. X. Tang, "Ultra-high-Q UV microring resonators based on a single-crystalline AlN platform," *Optica* **5**(10), 1279–1282 (2018).
44. Q. Zhao, M. W. Harrington, A. Isichenko, K. Liu, R. O. Behunin, R. O. Behunin, S. B. Papp, P. T. Rakich, C. W. Hoyt, C. Fertig, and D. J. Blumenthal, "Integrated reference cavity with dual-mode optical thermometry for frequency correction," *Optica* **8**(11), 1481–1487 (2021).
45. S. M. Clark, D. Lobser, M. Revelle, C. G. Yale, D. Bossert, A. D. Burch, M. N. Chow, C. W. Hogle, M. Ivory, J. Pehr, B. Salzbrenner, D. Stick, W. Sweatt, J. M. Wilson, E. Winrow, and P. Maunz, "Engineering the Quantum Scientific Computing Open User Testbed (QSCOUT): Design details and user guide," arXiv:2104.00759 [quant-ph] (2021).
46. M. Saffman, "Quantum computing with atomic qubits and Rydberg interactions: progress and challenges," *J. Phys. B: At., Mol. Opt. Phys.* **49**(20), 202001 (2016).
47. J. F. Bauters, M. J. R. Heck, D. Dai, J. S. Barton, D. J. Blumenthal, and J. E. Bowers, "Ultralow-Loss Planar Si₃N₄ Waveguide Polarizers," *IEEE Photonics J.* **5**(1), 6600207 (2013).
48. M. Piels, J. F. Bauters, M. L. Davenport, M. J. R. Heck, and J. E. Bowers, "Low-Loss Silicon Nitride AWG Demultiplexer Heterogeneously Integrated With Hybrid III–V/Silicon Photodetectors," *J. Lightwave Technol.* **32**(4), 817–823 (2014).